

Direct measurements and path integral Monte Carlo calculations of kinetic energies of solid neon

D N Timms[†], A C Evans^{†+}, M Boninsegni[‡], D M Ceperley^{†§}, J Mayers^{||}
and R O Simmons^{§¶}

[†] Division of Physics, Portsmouth University, King Henry I Street, Portsmouth PO1 2DZ, UK

[‡] National Center for Supercomputing Applications, University of Illinois at Urbana-Champaign, 405 North Mathews Avenue, Urbana, IL 61801, USA

[§] Department of Physics, University of Illinois at Urbana-Champaign, 1110 West Green Street, Urbana, IL 61801-3080, USA

^{||} Rutherford Appleton Laboratory, Chilton, Didcot, Oxon, OX11 0QX, UK

[¶] Frederick Seitz Materials Research Laboratory, University of Illinois at Urbana-Champaign, 104 South Goodwin Avenue, Urbana, IL 61801, USA

Received 16 November 1995, in final form 9 May 1996

Abstract. Direct measurements are reported of the kinetic energies $\langle E_k \rangle$ of FCC neon at seven temperatures between 4.25 and 20.2 K. The measurements employed the electronvolt spectrometer which is the neutron scattering instrument at the ISIS neutron source, UK. Wavevector transfers Q from 306 to 1158 nm⁻¹ were used, far larger than previously, in a regime where possible final-state-effect corrections to the observed longitudinal neutron Compton profile $J(y)$ are easily dealt with by a simple correctional procedure. The results are of comparable precision with the best previous work, carried out using the HRMECS instrument at IPNS, Argonne. From those previous measurements, Peek *et al* give a ground-state kinetic energy of 49.1 ± 2.8 K. Path-integral Monte Carlo calculations were performed using both HFD-C2 and Lennard-Jones pair potentials. At 4.13 K, 10.13 K, 15.69 K and 20.31 K the HFD results were 41.6 ± 0.1 K, 42.6 ± 0.1 K, 46.5 ± 0.1 K and 47.8 ± 0.1 K, respectively. These values are broadly in agreement with the current measurements. They are significantly lower than the published values obtained from an HFD-based Wigner–Kirkwood high-temperature expansion including terms up to \hbar^6 .

1. Introduction

Neutron Compton scattering (NCS) is an experimental technique which can be used to probe directly the ground-state momentum distribution $n(p)$ of atoms in condensed matter. The technique was first suggested almost 30 years ago [1] and it is analogous to the measurement of electron momentum by photon Compton scattering [2]. As with Compton scattering, the interpretation is based on the validity of the impulse approximation (IA) which is exact when both the energy and the momentum transferred to the target are infinite [3]. Deviations from impulsive scattering occur at finite values of Q and are referred to as final-state effects (FSE) [4]. The question of when the IA may be deemed valid is still a matter of debate although it is agreed that FSEs become smaller at higher Q [5]. High-momentum transfers can be achieved with inverse geometry spectrometers receiving high-energy neutrons from pulsed-spallation neutron sources [6], which unlike reactors provide sufficient flux at the incident energies required, 10^{-1} – 10^2 eV.

⁺ Present address: UG7, Building R3, Rutherford Appleton Laboratory, Chilton, Didcot, OX11 0QX, UK.

Knowledge of $n(\mathbf{p})$ permits scalar properties such as the average kinetic energy $\langle E_k \rangle$ to be known, potentially on a par with fundamental macroscopic thermodynamic properties such as P - V - T relations and heat capacity. The NCS technique has already proved successful in determining atomic momentum distributions and in obtaining directly values for the mean atomic kinetic energies of a number of light elements, e.g. liquid and solid hydrogen [7], hydrogen-bonded materials [8], solid [9] and liquid [10] helium, other noble gases in both solid and liquid phases [11–13], metals [14] and graphite [15]. Moreover, because the centres of the observed recoil peaks are separated kinematically by nuclear mass differences, the NCS technique can selectively probe the dynamical characteristics of particular atomic species in complicated systems, e.g. in metal hydrides [16] and glasses [17].

Condensed neon is of particular interest as it is not a pure quantum system such as helium nor does it behave classically as do the other noble-gas systems at high temperatures. In both liquid and solid argon, krypton and xenon the momentum distributions are given by the Maxwell–Boltzmann distribution, namely a Gaussian with a width related to the kinetic energy [18]. In neon the shape of $n(\mathbf{p})$ is still Gaussian but quantum effects are manifest as an increase in the measured values of the kinetic energy above the classical expectation [13]. Solid neon was chosen for the present work as it is a simple system for which firstly, given an interatomic potential, a rigorous calculation of $\langle E_k \rangle$ is possible, secondly the distribution $n(\mathbf{p})$ had not been measured at very large wavevector transfers Q and thirdly other experimental data are available for comparison. Inelastic neutron scattering experiments have been performed [12] with energy transfers in the electronvolt regime on solid natural neon at five temperatures between 4.7 and 26.4 K and at pressures between equilibrium vapour pressure and 17.6 MPa. They compared measurements of $\langle E_k \rangle$ with existing theoretical calculations and showed that none of these predicted their observed ground-state kinetic energy. These experiments were carried out within the IA but at energy and momentum transfers where FSEs were significant. In this paper we report measurements of the mean atomic kinetic energy of solid neon performed at energy and momentum transfers much larger than those reached in previous measurements. Under these conditions, corrections for FSEs are unnecessary and a more reliable comparison with theory can be made. Our data are compared with both path-integral Monte Carlo (PIMC) calculations carried out using two different two-body interatomic potentials for temperatures and pressures close to the experimental conditions and with previous measurements of $\langle E_k \rangle$.

In section 2 we recall the basic theory of NCS from a monatomic system; in section 3 we describe an experimental technique for measuring the inelastic scattering of neutrons at very large Q and detail the conditions of our scattering samples. Section 4 describes the analysis procedure, including (section 4.2) consideration of the difference between $S(Q, E)$ and $S_{IA}(Q, E)$ for finite Q . Section 5 describes the calculations performed on solid neon, to produce $\langle E_k \rangle$ -values with which the measurements are directly compared. We conclude with comments, section 6, on the current state of the art of obtaining $n(\mathbf{p})$ from measurements at very high Q and of obtaining $\langle E_k \rangle$ from rigorous theory.

2. Neutron scattering theory

The inelastic differential cross section for scattering of neutrons by N identical scatterers of mass m can be written [19]

$$\frac{d^2\sigma}{d\Omega dE} = Nb^2 \left(\frac{k_f}{k_i} \right) S(Q, E) \quad (1)$$

where b is a scattering length, k_i and k_f are the magnitudes of the initial and final neutron wavevectors, respectively,

$$Q = k_i - k_f \quad (2)$$

and

$$E = \frac{\hbar^2}{2m}(k_i^2 - k_f^2) \quad (3)$$

is the energy transfer. The dynamic structure factor $S(\mathbf{Q}, E)$ has the form

$$S(\mathbf{Q}, E) = \frac{1}{2\pi\hbar} \int_{-\infty}^{\infty} I(\mathbf{Q}, t) \exp\left(-\frac{iEt}{\hbar}\right) dt. \quad (4)$$

The intermediate scattering function $I(\mathbf{Q}, t)$ is the sum of a thermodynamic average:

$$I(\mathbf{Q}, t) = \frac{1}{N} \sum_{ij} \langle \exp\{-i\mathbf{Q} \cdot \mathbf{r}_i(0)\} \exp\{i\mathbf{Q} \cdot \mathbf{r}_j(t)\} \rangle \quad (5)$$

where \mathbf{r}_i and \mathbf{r}_j are atomic position operators.

In the extreme limit of large Q when incident neutrons scatter incoherently and independently from individual nuclei, $S(\mathbf{Q}, E)$ becomes proportional to $n(\mathbf{p})$.

$$S(\mathbf{Q}, E) \rightarrow S_{IA}(\mathbf{Q}, E) = \int_{-\infty}^{\infty} n(\mathbf{p}) \delta\left(E - E_r - \frac{\hbar}{m} \mathbf{Q} \cdot \mathbf{p}\right) d\mathbf{p} \quad (6)$$

with $n(\mathbf{p})$ normalized to unity and the recoil energy is $E_r = \hbar^2 Q^2 / 2m$. In this limit, with the z axis along Q , equation (6) can be written [20]

$$S_{IA}(\mathbf{Q}, E) = \frac{m}{\hbar Q} J(y) \quad (7)$$

where the scaling variable is

$$y = \frac{m}{\hbar Q} (E - E_r) \quad (8)$$

and the 'longitudinal neutron Compton profile' is

$$J(y) = \int_{-\infty}^{\infty} n(p_x, p_y, y) dp_x dp_y. \quad (9)$$

The neutron Compton profile $J(y)$, like $n(\mathbf{p})$, is also normalized. For an isotropic sample such as a liquid or a polycrystalline solid, $n(\mathbf{p}) = n(p)$ and the orientation of Q with respect to the scattering sample is immaterial. Hereafter, we omit vector designation of p and of Q .

3. Experimental arrangements

3.1. The neutron electronvolt spectrometer

The electronvolt spectrometer (eVS) at the UK pulsed-neutron source ISIS, Rutherford Appleton Laboratory, was specifically developed for the direct measurement of atomic momentum distributions and is equally suited to the study of both low- and high-mass systems [21]. In this work, two independent measurements, referred to as measurements A and B, were made using different spectrometer configurations but the same sample conditions. A full description of the eVS and of a typical spectrometer configuration can be found in the literature [22, 23] and only a brief description is given here.

The eVS receives a broad continuous-energy spectrum of incident neutrons in pulses at 50 Hz, from the ambient water moderator which is situated near the ISIS tantalum target. Detectors at fixed angles ϕ register neutron spectra as the neutron time of flight (TOF) from the moderator. Two types of neutron detector were used in measurement A: ^3He gas detectors and recently installed lithium-doped glass scintillator detectors. The intrinsic properties of the gas detectors are well understood but their efficiency is almost an order of magnitude lower than that offered by the scintillator detectors. Measurement B was undertaken 18 months later, by which time only higher-efficiency scintillation detectors were in use. The aim of measurement B was to investigate the Q dependence of the FSEs in neon; however, as we shall show, FSEs were not present above the statistical accuracy of either data set. The $\langle E_k \rangle$ -values obtained from measurement B are included here as they demonstrate the experimental consistency offered by the eVS and its analysis routines.

The final energy of scattered neutrons is fixed by a nuclear resonant filter-difference technique. Thin metal foils in the scattered neutron paths absorb neutrons having energies $\hbar^2 k_f^2 / 2m_n$ centred at the nuclear resonance energies, m_n is the neutron mass. Gold (^{197}Au) and uranium (^{238}U) analyser foils of thickness $10\ \mu\text{m}$ and $30\ \mu\text{m}$, respectively, were used in this study. When the foils are removed from the scattered beam, the total spectrum is available for subtractions. The neutron TOF over the incident flight path from the moderator gives the incident energy $\hbar^2 k_i^2 / 2m_n$ and the magnitude of the wavevector transfer is given by

$$Q = (k_i^2 + k_f^2 - 2k_i k_f \cos \phi)^{1/2}. \quad (10)$$

The accuracy of the method depends upon the choice of resonance filter, upon precise knowledge of its properties, upon reliable data normalization, and upon accurate calibration of instrument geometry [24, 25]. Significant effort has been directed towards the complete characterization of the instrument and some earlier experimental anomalies can now be attributed to uncertainties in the data analysis procedure. For example, the observed disagreement between a Debye model of the kinetic energy of lithium and that observed in an early measurement of lithium has now been attributed to a deficiency in the early data analysis [23].

The energies and energy widths of the nuclear resonances used were obtained from measurements of the recoil scattering from the elements Pb, V, Al and Be. The peak cross sections σ_E of the resonances (taking into account Doppler broadening) were obtained from tables [26, 27] and are listed in table 1. The angular range of each detector module and the corresponding wave-vector transfer for each nuclear resonance and detector module combination are also shown in table 1. The three nuclear resonances of uranium, used to define the scattered beam energy, are sufficiently well separated from one another to avoid the overlap of the scattering from the neon sample and the vanadium container. The resonance foils were automatically cycled in and out of the scattered beams every 5 min to minimize possible systematic errors arising from time variation in the efficiencies of the detector systems. For measurement A, gold foils were used in conjunction with one of two banks of ten ^3He gas detectors at back-scattering angles and with both banks of ten ^3He gas detectors at forward-scattering angles. Uranium foils were used in conjunction with the other bank of ten ^3He gas detectors at back scattering in TOF and a bank of eight glass scintillator detectors placed at intermediate scattering. For measurement B, uranium foils were used in conjunction with two banks of eight scintillator detectors placed symmetrically about the incident beam at intermediate scattering angles and two banks were placed at back-scattering angles. The difference spectra (foil out – foil in) were normalized by comparison of their respective integrals over the TOF region from 500 to 600 μs . This is an interval

unaffected by the analyser foil resonances and near to the region of interest around the recoil peak. It is more accurate than use of the respective monitor counts, which can show a few per cent variability.

Table 1. Energies E_R and Lorentzian resolution widths σ_E of the nuclear resonance absorption peaks used. Values for E_R were deduced from the instrument calibration and the corresponding σ_E -values were obtained from tables taken from [26,27]. They take into account Doppler broadening of the absorption resonance lineshape and are valid at 295 K.

Analyser foil	E_R (meV)	σ_E (\AA^{-1})	Measurement A		Measurement B	
			Nominal detector angle (deg)	Wavevector transfer for ^{20}Ne (\AA^{-1})	Nominal detector angle (deg)	Wavevector transfer for ^{20}Ne (\AA^{-1})
^{197}Au	4922 ± 142	36 583	36.2–54.0 141.0–153.0	30.5–44.7 44.7–96.2		
^{238}U	6671 ± 163	21 790	105.4–129.2 141.4–153.5	93.3–107.0 112.2–116.1	91.6–117.6 124.7–150.3	83.5–100.8 104.7–115.1
^{238}U	20872 ± 131	32 242	105.4–129.2 141.4–153.5	165.1–189.4 198.6–205.5	91.6–117.6 124.7–150.3	147.7–178.4 185.2–203.7
^{238}U	36680 ± 223	40 253	105.4–129.2 141.4–153.5	219.0–251.1 263.4–272.5	91.6–117.6 124.7–150.3	195.4–236.4 245.5–270.0

To determine kinetic energies from the measured spectra it is necessary to account for the resolution contribution in y space for each individual detector. Analytical expressions for the components of the instrument resolution have been given in a previous paper [24]. There are five independent contributions to the y -space resolution. These arise from uncertainties in the measured TOF, the distribution in the initial and final flight paths, the scattering angles and the energy values allowed by the instrument geometry and analyser foil resolution. In each measurement the instrument geometry was calibrated by analysis of diffraction from a slab sample of polycrystalline Pb and of recoil scattering by Pb, V, Al and Be (corrected for inelasticity), with a U foil placed in the incident beam. The U foil was placed well away from the detectors in order to avoid spurious scattering. First the total flight path including delay time to each detector was determined from the position of the resonance absorption lines. Then these quantities were used to calculate the scattering angles for each detector using the positions of the four longest d -spacing Pb Bragg peaks. This procedure has been explained in detail elsewhere [25]. In each case, a recoil correction was made. The resolution of the eVS is dominated by the intrinsic energy width of the analyser foil nuclei used. This function was previously determined for each detector both analytically and experimentally by measurements of the recoil scattering from heavy systems such as Pb and Sn and, in the case of gold, the absorption is well represented by the following Lorentzian expression:

$$R_E(y) = \frac{\text{constant}}{y^2 + \sigma_E^2} \quad (11)$$

where σ_E is the width of the Lorentzian resolution function $R_E(y)$. In the case of the U analyser foil, the absorption cross section for a sufficiently thin foil (less than $50 \mu\text{m}$) is well represented by a Gaussian function. This is because the intrinsic lineshape is dominated by thermal Doppler broadening at room temperature. The angular resolution is small except for scattering from hydrogenous systems and was determined for all detectors by a Monte Carlo calculation. Relatively small geometric resolution contributions arise from the angular width

of a given detector, from the depth of the neutron moderator, and from the distribution of incident- and scattered-neutron path lengths. These geometric contributions are determined by a standard calculation procedure [21]. All resolution components except that from the Lorentzian resonance of gold are well described by Gaussian functions. The resultant resolution function for a gold analyser is therefore a Voigt function, i.e. a convolution of a Gaussian and a Lorentzian, and that for a U analyser foil is a Gaussian.

In general the scattered flight path is large compared with the detector height and the geometrical component of the resolution resulting from the TOF range offered by the finite detector height can be neglected. Limited beam time was available for measurement B and count rates were maximized by placing the detector banks close to the sample. Unfortunately the additional geometrical resolution was found to be both complicated and significant at back scattering and could not be successfully removed from these data. Fortunately the resolution effect is strongly dependent on the scattering angle and was not detectable in the smaller-angle data and only these data are presented here.

Table 2 lists the resolution components for detectors in the middle of each detector bank for measurement A. It is clear that, in each case, the dominant contribution arises from the foil resonance and that the narrowest resolution can be obtained from the scintillator detectors with the uranium foil at intermediate scattering. These data offer the most accurate and reliable measurement of the kinetic energy. The remaining data provide useful checks on the data analysis procedures and instrument calibration. Furthermore, the use of both U and Au foils in the various detector banks in measurement A, as shown, made possible a variety of cross checks for possible systematic errors.

Table 2. Momentum resolution components Δy for the eVS detectors in the centre of each detector bank in measurement A. All values listed are Gaussian standard deviations except the Lorentzian contribution from the gold resonance which is listed as HWHM. The subscripts θ , t , l_0 , l_1 and E_R relate to the contributions from variations in the scattering angle, time binning, incident and scattered flight paths and the appropriate nuclear resonance. The total Gaussian and Lorentzian resolution widths and the widths of each resonance are also given.

Detector	Foil	θ (deg)	E_R (meV)	ΔE_R (meV)	Δy_θ (\AA^{-1})	Δy (\AA^{-1})	Δy_{l_0} (\AA^{-1})	Δy_{l_1} (\AA^{-1})	Δy_{E_R} (\AA^{-1})	Gaussian total (\AA^{-1})	Lorentzian total (\AA^{-1})
Scintillation	U	117	6671	63	0.765	0.717	1.308	1.138	3.380	3.941	
Scintillation	U	117	20872	131	1.353	2.244	2.313	2.013	3.973	5.662	
Scintillation	U	117	36680	223	1.794	3.944	3.066	2.668	5.102	7.831	
Gas	Au	147	6671	63	0.159	3.156	1.222	0.853	3.175	4.721	
Gas	Au	147	20872	131	0.280	9.874	2.161	1.509	3.732	10.883	
Gas	Au	147	36680	223	0.372	17.353	2.864	2.000	4.792	18.342	
Gas	Au	147	4922	142	0.137	2.330	1.050	0.733	8.348	2.662	8.348
Gas	Au	45	4922	142	0.481	5.285	2.576	1.663	20.132	6.129	20.132

At long TOF (say, $t > 2000 \mu\text{s}$), eVS spectra show peaks resulting from neutron diffraction by the sample. These data are collected simultaneously with the inelastic data. It is important to know the density of the samples in order to make comparisons with previous experiments and calculations, since $\langle E_k \rangle$ is a function of temperature and pressure (or volume). In the current measurements, good use was made of this facility in the preparation and characterization of neon (section 3.2).

3.2. Sample characterization

For both measurement A and measurement B, the natural neon samples [28] were contained in a V cell about 23 mm wide and 3 mm thick, having a wall thickness of 0.05 mm. The cross section of the incident neutron beam was a circle of 50 mm diameter with a 30 mm umbra centred on the cell. Cell temperatures were maintained in the sample space of an ‘orange’ cryostat [29], which provided ^4He exchange gas at about 1 kPa in a radiant and physical environment within 0.1 K of the cell temperature. The cell temperature was maintained constant to within ± 0.05 K during each measurement. The solid neon samples were held at a low pressure via an open vertical capillary of 0.5 mm ID, connected to pressure gauges and a ballast volume, all at room temperature, and constituting a total volume of about 1 litre. The observed pressure varied in the range 30–60 kPa, depending on the level of the liquid neon maintained in the capillary. The solid neon was prepared by first liquefying the sample and then further cooling the sample cell while more neon sample gas was added. For measurement A the solid samples were run in order: at 10.2 K, then at 4.25 K and finally at 20.2 K. For measurement B the sample temperatures were 4.34, 10.8, 15.2 and 20.1 K. In both measurements a reference empty cell was run at 20 K. Sample thermometer calibration was checked approximately by the observation of thermal arrest during sample phase change and at the end of data collection.

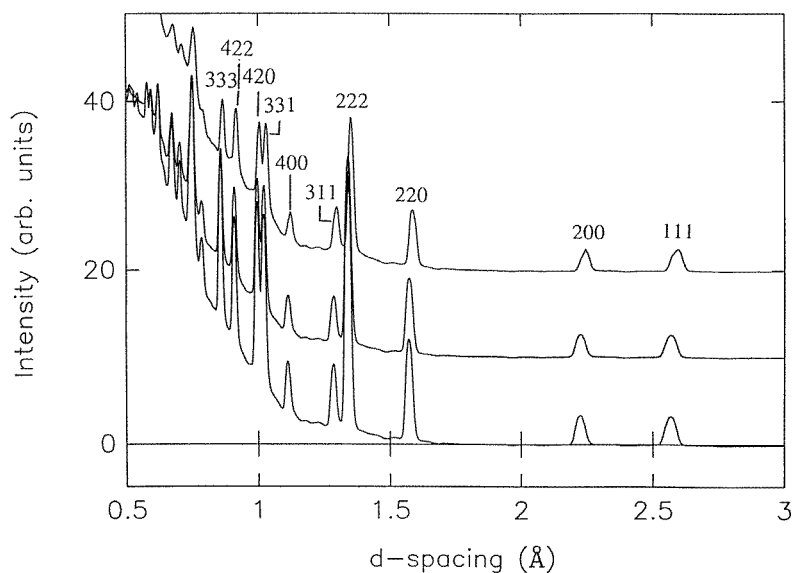


Figure 1. Examples of diffraction data obtained in measurement A with the scintillator detectors at temperatures of 4.25 K, 10.2 K and 20.2 K. The data have been converted from TOF to d space. All allowed FCC diffraction peaks (111) to (333) are observed, indicating that a good degree of polycrystallinity was obtained.

Neutron Compton profile measurements of polycrystalline samples provide the isotropic average of the longitudinal neutron Compton profile, equation (9). Examples of the eVS diffraction spectra obtained in measurement A with the scintillator detectors at temperatures of 4.25, 10.2 and 20.2 K are shown in figure 1. These spectra were scrutinized, detector by detector, for differences which would indicate the degree of polycrystallinity, extent of any preferred orientation, etc. The diffraction data have been converted from TOF to d

Table 3. Properties of the natural neon samples. The density values were calculated from x-ray measurements.

Measurement	T (K)	Lattice parameter expected [30] (nm)	Lattice parameter measured (nm)	Density (atoms nm ⁻³)
A	4.25	0.446 38(1)	0.445 50(5)	44.97
A	10.20	0.446 80(1)	0.447 34(4)	44.85
A	20.20	0.450 52(1)	0.449 96(5)	43.78
B	4.34	0.446 38(1)	0.444 52(5)	44.97
B	10.8	0.446 91(1)	0.444 71(5)	44.81
B	15.2	0.448 11(1)	0.446 66(5)	44.45
B	20.1	0.450 45(1)	0.448 73(5)	43.76

space. The data showed no indications of directional dependence. The measured lattice parameters, the expected values [30] and the calculated sample densities are shown in table 3. All allowed FCC diffraction peaks (111) to (333) were seen. There is very good agreement between the observed lattice parameters and those expected for all temperatures measured. This indicates both that the sample temperatures are accurately known, because of the very large thermal expansion coefficient of solid neon, and that the samples were not constrained within the cell.

4. Experimental analysis and results

4.1. Basic analysis

The data analysis procedures for eVS have been described fully elsewhere [21, 25] and only a summary is given here. Data sets were obtained simultaneously for a variety of different combinations of detector type, analyser resonances and scattering angles. This diversity provides a valuable check on the analysis procedure and helps to identify the source and hence to reduce the effect of systematic errors.

For each neon sample in measurement A, about 6.2×10^6 scattered neutrons were recorded with the ³He gas detectors whereas 1.5×10^8 scattered neutrons were recorded with the higher-efficiency scintillator detectors. These figures correspond to about 20 h running time (3400 μ a h of ISIS proton beam). In measurement B, 8.0×10^8 scattered neutrons were recorded in 22 h running time (3800 μ a h). The ‘foil in’ and ‘foil out’ TOF spectra from each detector were normalized and then subtracted. The total scattering comes both from the sample and from the vanadium sample can, thermal and vacuum windows in the cryostat, etc. Our analysis is principally focused on the dominant scattering by the ²⁰Ne nuclei (over 90%, (table 4)). With the sample removed, the residual background can be determined with high precision. The normalization procedure was repeated for the empty sample-can data which were then subtracted from each data spectrum. The resulting differenced TOF spectrum for each detector yielded those neutrons which were captured by the resonant foil after scattering through the angle defined by that detector. The ²¹Ne and ²²Ne scattering contributions were removed by modelling the scattering in the TOF spectrum. The relative scattering power for each isotope was determined from the relative abundance and scattering cross-section (see table 4) and a least-squares fit was made to the neon recoil peaks in the TOF spectrum using the expression

$$S(t) = R(T) \otimes [aG(s_{22}, t - t_{22}) + bG(s_{21}, t - t_{21}) + cG(s_{20}, t - t_{20})]A \quad (12)$$

Table 4. Properties of neon isotopes.

Isotope	Relative abundance [31] (%)	Mass (amu)	Scattering cross section [32] (bn)	Relative scattering intensity (%)
^{20}Ne	90.48(3)	19.9924	2.671(14)	92.7
^{21}Ne	0.27(1)	20.9938	5.6(3)	0.6
^{22}Ne	9.25(3)	21.9914	1.88(1)	6.7

where $S(t)$ is the measured spectrum, A is a scaling factor, \otimes signifies a convolution, $R(t)$ is the instrument resolution function and the constants a , b and c are the relative scattering powers of the ^{22}Ne , ^{21}Ne and ^{20}Ne nuclei, respectively. The functions $G()$ are Gaussians centred at the IA recoil position where t_{22} , t_{21} and t_{20} are the recoil peak positions for the corresponding neon isotopes. The ratios of the Gaussian variances σ_{22} , σ_{21} and σ_{20} were scaled to the ratio of the fourth root of the corresponding isotopic mass. Figure 2 shows an example of one of the TOF spectra collected with the scintillation data for the run at 4.25 K. The three Gaussian contributions are shown together with the sum which is a good fit to the experimental data. The ^{22}Ne and ^{21}Ne scattering contributions were subtracted in the TOF spectrum and each differenced spectrum was transformed into momentum space using equation (8) and an atomic mass of 20 amu.

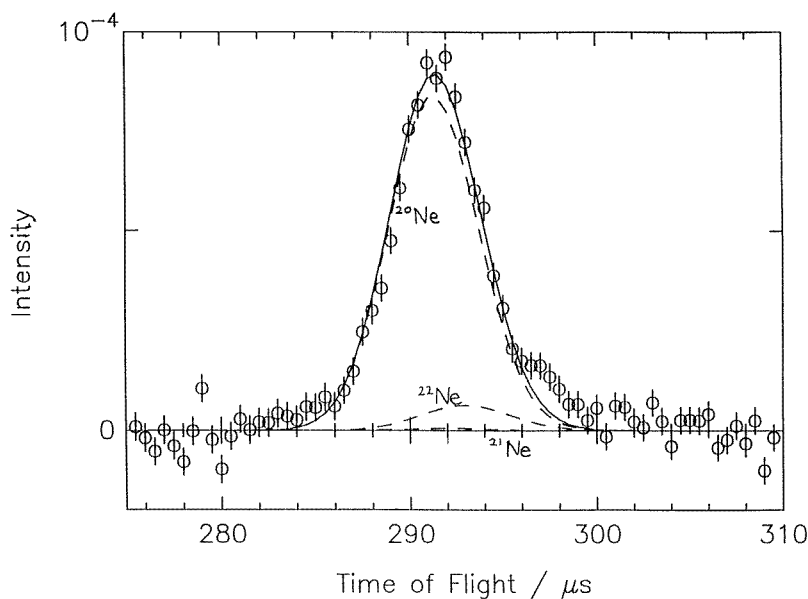


Figure 2. A typical TOF spectrum obtained from one of the scintillator detectors. The scattering angle was 105.3° and the sample temperature was 4.25 K. The data display a feature at 280–300 μs corresponding to the superposition of ^{20}Ne , ^{21}Ne and ^{22}Ne scattering contributions. The small feature centred at 297 μs is due to the recoil scattering from the vanadium sample holder. The ^{20}Ne , ^{21}Ne and ^{22}Ne scattering contributions are represented by the broken curves and the solid curve represents the sum of these three.

Neutron Compton profiles obtained from FCC ^{20}Ne at 4.25 K from a variety of different combinations of absorber resonance, detector type and scattering angle are shown in figure 3.

In each case the instrument resolution function is included for comparison. The highest-resolution data are obtained from detectors at back-scattering angles and the 6671 meV resonance of U. This sequence of plots clearly shows that the scintillator detectors offer a more accurate measurement of $\langle E_k \rangle$ than that offered by the gas detectors and with a better resolution. In each case the data have been fitted by the appropriate Voigt or Gaussian function. When results of high precision are desired, it becomes necessary to consider the possible influence that sample-dependent multiple scattering may have upon the derived spectra. In the present work, we have not attempted to simulate this effect by Monte Carlo means; rather we have relied upon the use of a 'thin' sample and sample can and cross checking results from different angles to ensure that the effects are indeed negligible. Our neon sample and the thin sample cell used scattered about 1% and 2%, respectively, of the incident beam. It is expected that the sample-dependent multiple scattering will give differing contributions to spectra observed for different scattering angles, so that comparison of spectra for the different detectors will give an indication of its significance, if any, in the final results. A comparison of figure 3(a) with figure 3(d) confirms that sample-dependent multiple scattering, which would be manifest as a broad peak at y -values to the right of the peak, is indeed negligible.

Over 9% of the scattering from the neon sample is from ^{22}Ne (see table 4) and so an attempt was made to isolate the scattering from this component by fitting to the recoil peak in the manner explained above, and subtracting the contributions from ^{20}Ne and ^{21}Ne . The resulting TOF spectra were too noisy and were not of sufficient quality to merit any further analysis.

As the filter-difference method employs an intense broad spectrum of incident neutrons, it is not well adapted for precise study of relatively weak scattering in the extreme wings of $J(y)$ because the counting statistics over the entire range of $J(y)$ are essentially constant. Neutron Compton scattering from condensed neon is expected to be essentially that from a single Gaussian $n(p)$ and this assumption is made throughout our analysis. The present work also is a critical test of the stability and consistency of measurements made with eVS under various experimental conditions.

4.2. Correction for final-state effects

Owing to the extremely large wavevector transfers used in the present work (table 1 and figures 3(a)–3(d)), FSEs to these data are expected to be very small. Nevertheless, the high precision of the present data justifies explicit consideration of this small correction.

For present purposes, we write $S(Q, E)$ as the sum of symmetric ($S_s(Q, E)$) and antisymmetric ($S_a(Q, E)$) parts, respectively [33]:

$$S_s(Q, E) = \frac{m}{\hbar Q} \left[1 + A_4(Q) \frac{d^4}{dy^4} \right] J(y) \quad (13)$$

and

$$S_a(Q, E) = \frac{m}{\hbar Q} \left[-A_3(Q) \frac{d^3}{dy^3} \right] J(y). \quad (14)$$

In these equations, only the leading correction to the IA is retained in each case because, at larger Q , A_3 decreases as Q^{-1} and A_4 decreases as Q^{-2} . Explicitly,

$$A_3 = \frac{m \nabla^2 V}{36 \hbar Q} \quad (15)$$

and

$$A_4 = \frac{m^2 \langle \mathbf{F}^2 \rangle}{72 \hbar^4 Q^2} \quad (16)$$

where V is the potential and \mathbf{F} is the force on an atom. Also explicitly,

$$\langle \nabla^2 V(r) \rangle = 4\pi\rho \int \nabla^2 V(r)g(r)r^2 dr \quad (17)$$

where $g(r)$ is the pair distribution function.

In the range of the present work, $30.5 \text{ \AA}^{-1} < Q < 272.5 \text{ \AA}^{-1}$, the magnitude of A_3 is at most 10% of that expected in the data [34] analysed by Sears [35]. Moreover, those data [34] contain visible oscillations in the width of $S(Q, E)$ which, while interesting as possible interatomic interference effects, are an obstacle to unambiguous removal of FSEs by this method. Our values of $\langle E_k \rangle$, *without* FSE correction, are presented in table 5 for solid neon. Our resolution-broadened measurements can be well fitted by a symmetric Voigt function or Gaussian function (as appropriate); hence we assume that any effects on the deduced $\langle E_k \rangle$ -values by an A_3 contribution are negligible. One expects in any case that coupling of an antisymmetric component to determination of a peak width is small. We select the $\langle E_k \rangle$ -values determined from the data collected in measurement A with the U foil and scintillation detectors as being the most reliable. We do this mainly because this combination of analyser foil–detector–scattering angle offers the most favourable resolution. The statistical accuracy of these data is better than that obtained in measurement B and is the consequence of the limited run time available for this measurement.

Table 5. Deduced values of the kinetic energy of FCC neon. For the present experimental work, deduced values apply to ^{20}Ne in the natural mixture.

Experimental measurements			
Density (nm^{-3})	Temperature (K)	$\langle E_k(\rho, T) \rangle$ (K)	Reference
44.97	4.25(5)	44(1)	Present experiment A
44.97	4.34(5)	44(3)	Present experiment B
44.97	4.7(1)	49(3)	Peek <i>et al</i>
44.26	9.4(1)	49(4)	Peek <i>et al</i>
44.68	10.2(1)	43(1)	Present experiment A
44.81	10.8(1)	45(5)	Present experiment B
44.77	11.4(2)	49(3)	Peek <i>et al</i>
44.45	15.2(1)	50(3)	Present experiment B
44.12	17.8(2)	51(3)	Peek <i>et al</i>
43.76	20.1(1)	48(3)	Present experiment B
43.91	20.2(1)	48(1)	Present experiment A

It is worth considering symmetrization of the measured neutron Compton profile in order to remove effects caused by the asymmetric component due to the A_3 term. One factor in deciding whether to do this is the size of the effect. For the more accurate uranium resonance–scintillation data combination we estimate the effect of the A_3 term would be to reduce the extracted $\langle E_k \rangle$ by an amount less than the statistical accuracy of these data. Furthermore, the extent to which symmetrization broadens the extracted value of σ depends strongly on the position in y space about which the data are symmetrized. Ideally the value $y = 0$ should be chosen, but small calibration errors can affect the true position of the

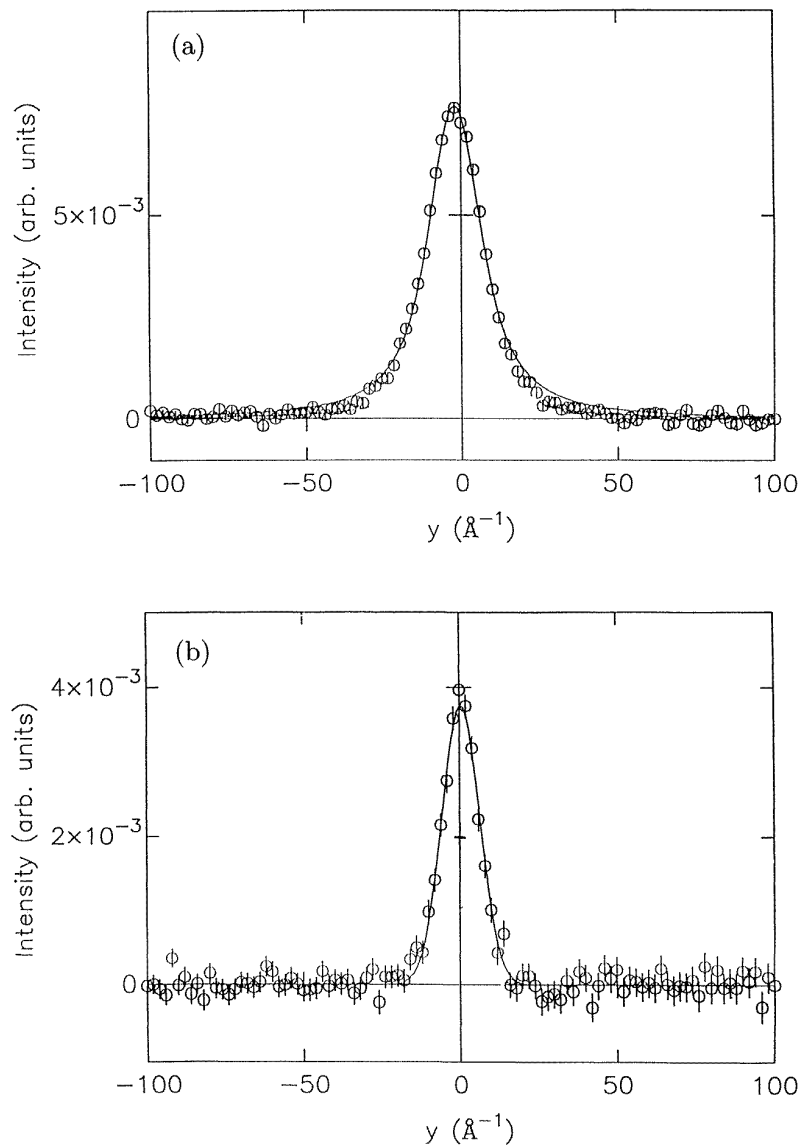


Figure 3. Neutron Compton profiles obtained from FCC neon at 4.25 K. In all cases the experimental points (\circ) have been converted to $J(y)$. They have been fitted (—) to a convolution of the resolution function (listed in table 2) with a Gaussian: (a) data for 145° gas-detector bank and Au foil (4922 meV). (b) data for 145° gas-detector bank and U foil (6671 meV) (note that the U resolution is narrower); (c) data for 145° gas-detector bank and U foil (36380 meV) (these data are dominated by the resolution broadening); (d) data for 117° scintillator-detector bank and U foil (6671 meV) (these data have much higher statistical precision than those from the gas detectors because of the high efficiency of this detector).

centre of the recoil peak. We conclude that, in this case, symmetrization of the data is not worthwhile.

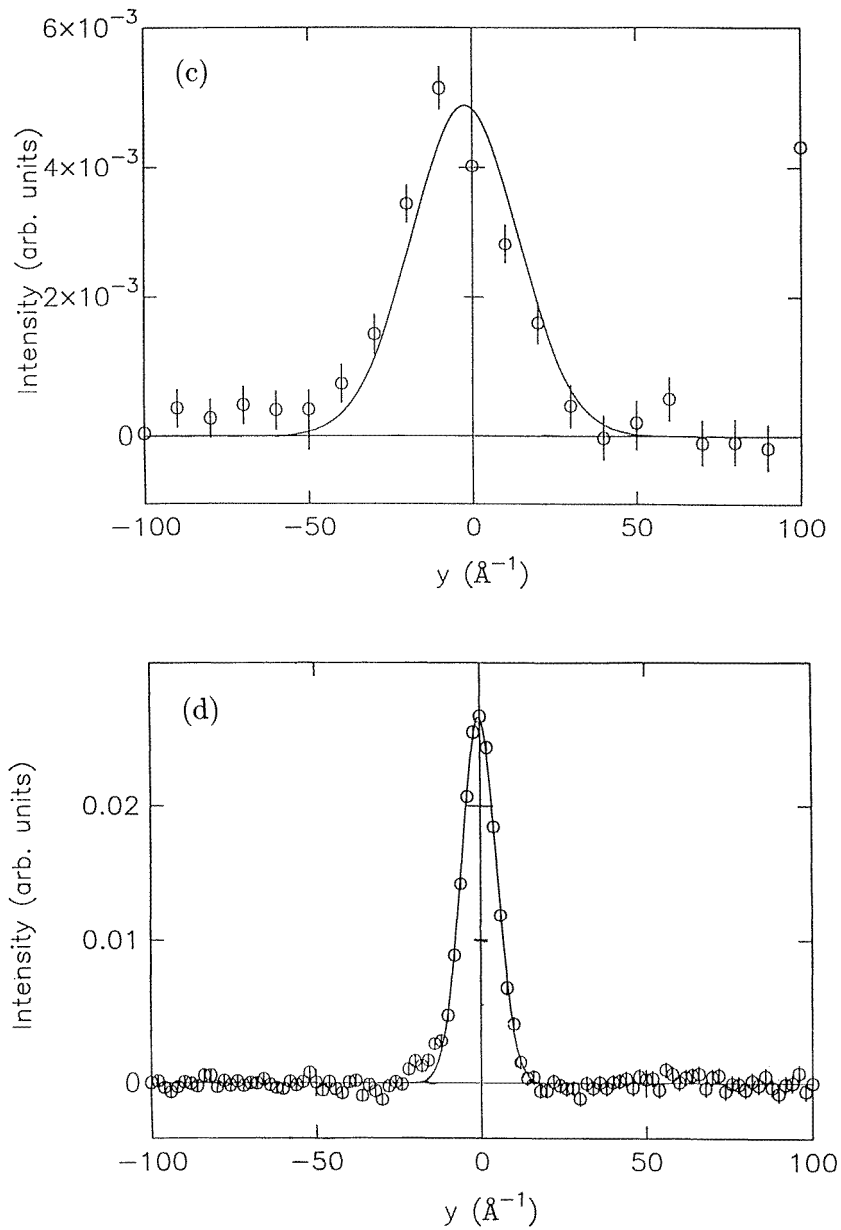


Figure 3. (Continued)

4.3. Comparison with previous experiments

The relation between the $J(y)$ distributions (e.g. figures 3(a)–3(d)) and the average kinetic energies $\langle E_k \rangle$ is given by

$$\langle E_k \rangle = \frac{3\hbar^2\sigma^2}{2mk_B} \text{ (in K)} \quad (18)$$

where k_B is the Boltzmann constant. In figure 4 we show our values of $\langle E_k \rangle$ for solid neon along with those of Peek *et al* [12] which were obtained with a chopper spectrometer at much lower Q . The data due to Peek *et al* for solid neon are some 10% larger than the eVS data presented here. The source of this apparent systematic discrepancy is not clear. There are several possible factors, although their relative importances are difficult to ascertain. In searching for possible systematic errors, Peek *et al* used different data analyses, analytical versus numerical, to account for data conversions from constant angle to constant Q . These two methods agreed, but it is now known that both are less satisfactory than full Monte Carlo simulation of the spectrometer [36]. Peek *et al* also used empirical fitting and subtraction of supposed multiple scattering (neon–neon and neon–sample can), with results which were later seen to be qualitatively different from Monte Carlo simulation [36]. Finally, FSE corrections by Peek *et al* used measured liquid $g(r)$ scaled from liquid data. The present PIMC $g(r)$ show some small but systematic offsets in r from those measurements. As pointed out by Peek *et al*, even in the presence of possible systematic errors in the absolute value of $\langle E_k \rangle$, relative values are more precise. We agree with the temperature dependence $\langle E_k(T) \rangle$ as found by Peek *et al*.

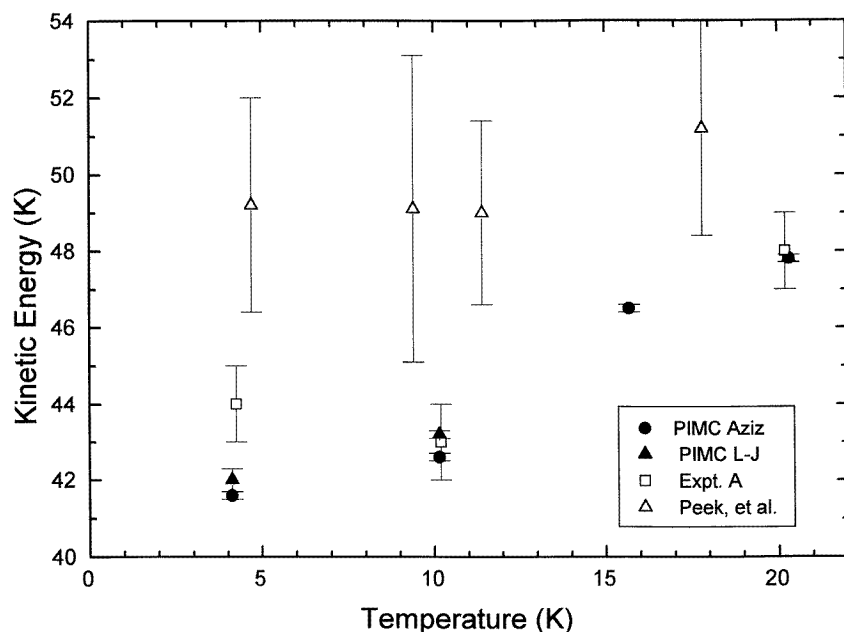


Figure 4. Values for $\langle E_k \rangle$ for solid neon obtained with the U foil and scintillator detectors in measurement A together with the data of Peek *et al* [12]. The new PIMC calculations using both the Lennard-Jones and the Aziz potentials are seen to be in agreement with the eVS data.

5. Path-integral Monte Carlo calculations

Published calculations of $\langle E_k(\rho, T) \rangle$ were listed by Peek *et al* in comparisons with their direct measurements on solid [12] and liquid neon [13]. Almost none of these calculations was specifically addressed to $\langle E_k(\rho, T) \rangle$ -values, and no quantitative agreement was found with measured values for any result of claimed high precision. Therefore, here we present

a rigorous model for condensed neon. The adequacy of a pair potential to model the atom–atom interaction in condensed neon can be tested theoretically by performing a PIMC simulation of an ensemble of neon atoms.

The PIMC technique is a powerful computational tool, affording quantitative studies of quantum many-particle systems at finite temperatures; it has proven remarkably successful in the investigation of complex Bose systems, such as superfluid ^4He [37]. In this work we utilize it to evaluate $\langle E_k(\rho, T) \rangle$ for solid neon, as well as to compute the pair distribution function $g(r)$, which is needed to calculate $\langle \nabla^2 V \rangle$ (equation (17)). Because there exist comprehensive review articles where this method is thoroughly described (see, e.g., [38]), we only sketch here its essential elements and discuss the aspects that are most relevant to the problem of interest. Given a quantum system of N particles, characterized by a Hamiltonian H , one can evaluate the thermodynamic average of a physical observable O for the system in thermal equilibrium at a temperature T as

$$\langle O \rangle = \frac{1}{Z} \int \int d\mathbf{R} d\mathbf{R}' O(\mathbf{R}, \mathbf{R}') \rho(\mathbf{R}, \mathbf{R}'; \beta) \quad (19)$$

where $|\mathbf{R}\rangle \equiv |r_1, r_2, \dots, r_N\rangle$ is a configuration ket specified by the position of all N particles, $O(\mathbf{R}, \mathbf{R}') = \langle \mathbf{R} | O | \mathbf{R}' \rangle$, $\rho(\mathbf{R}, \mathbf{R}') = \langle \mathbf{R} | \exp(-\beta H) | \mathbf{R}' \rangle$ (with $\beta = 1/k_B T$) is the many-body density matrix and $Z = \int d\mathbf{R} \rho(\mathbf{R}, \mathbf{R}'; \beta)$ is the partition function. On writing $\exp(-\beta \hat{H}) = [\exp(-\tau \hat{H})]^M$, with $\beta = M\tau$, one can transform (19) into

$$\langle O \rangle = \frac{\int \cdots \int d\mathbf{R}_1 d\mathbf{R}_2, \dots, d\mathbf{R}_{M-1} \rho(\mathbf{R}, \mathbf{R}_1; \tau) \rho(\mathbf{R}_1, \mathbf{R}_2; \tau) \cdots \rho(\mathbf{R}_{M-1}, \mathbf{R}; \tau) O(\mathbf{R})}{\int \cdots \int d\mathbf{R}_1 d\mathbf{R}_2, \dots, d\mathbf{R}_{M-1} \rho(\mathbf{R}, \mathbf{R}_1; \tau) \rho(\mathbf{R}_1, \mathbf{R}_2; \tau) \cdots \rho(\mathbf{R}_{M-1}, \mathbf{R}; \tau)} \quad (20)$$

A PIMC calculation consists in generating stochastically a set of independent random walks (paths) through the configuration space. Each path originates at a different starting N -particle configuration \mathbf{R} and returns to it after visiting $M - 1$ other configurations $\mathbf{R}_1, \mathbf{R}_2, \dots, \mathbf{R}_{M-1}$. Provided that the walks be statistically drawn from a probability density proportional to $\rho(\mathbf{R}_1, \mathbf{R}_2; \tau) \cdots \rho(\mathbf{R}_{M-1}, \mathbf{R}_M; \tau)$, the quantity $\langle O \rangle$ can be evaluated as a statistical average of the values of the matrix elements $O(\mathbf{R}_1, \mathbf{R}_M)$. The main point is that, as M increases (i.e. as $\tau \rightarrow 0$), one can obtain an explicit approximation for $\rho(\mathbf{R}, \mathbf{R}'; \tau)$ and this allows the generation of the above-mentioned set of random walks, by means of difference procedures [38].

The number M of ‘slices’ in which the interval β must be partitioned for the product $\rho(\mathbf{R}_1, \mathbf{R}_2; \tau) \cdots \rho(\mathbf{R}_{M-1}, \mathbf{R}_M; \tau)$ to be a satisfactory approximation to $\rho(\mathbf{R}, \mathbf{R}'; \beta)$ depends on how accurate an approximation one can obtain for $\rho(\mathbf{R}, \mathbf{R}'; \tau)$. It is highly desirable to keep the number M down to a minimum (i.e. paths as short as possible), in order for the calculation to be efficient. To this aim, a remarkably effective form for $\rho(\mathbf{R}, \mathbf{R}'; \tau)$ is given by

$$\rho(\mathbf{R}, \mathbf{R}'; \tau) = \rho^{(0)}(\mathbf{R}, \mathbf{R}'; \tau) \exp \left[- \sum_{i < j} u(r_{ij}, r'_{ij}; \tau) \right] \quad (21)$$

where $\rho^{(0)}(\mathbf{R}, \mathbf{R}'; \tau)$ is the density matrix for a system of N free particles and u is defined to be exact for two interacting neon atoms; r_{ij} and r'_{ij} are the distances between two neon particles at two successive slices, separated by τ . Ceperley and Pollock [39] found that using the pair-product form, equation (21), for $\rho(\mathbf{R}, \mathbf{R}'; \tau)$ substantially improves the method, as it affords a much greater accuracy, particularly at low temperatures, than the so-called ‘primitive’, or semiclassical, approximation, which is the most commonly used approximation for $\rho(\mathbf{R}, \mathbf{R}'; \tau)$.

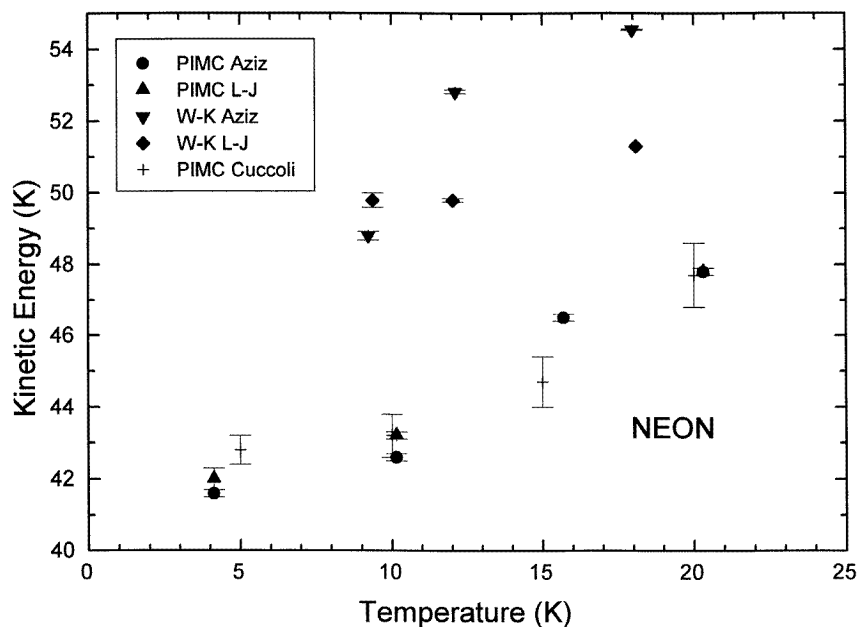


Figure 5. Here we compare our PIMC estimates for $\langle E_K \rangle$, obtained with both the Aziz HFD-C2 and the Lennard-Jones potential, with the theoretical results of Asger and Usmani who used a Wigner–Kirkwood expansion, and with the PIMC results of Cuccoli *et al*.

In this work we have performed a simulation of 108 neon atoms interacting via an accepted Aziz [40] HFD-C pair potential; for comparison purposes we also performed calculations with the Lennard-Jones potential [41]. We utilized the pair-product form equation (21) for the ‘high-temperature’ density matrix and observed evidence of convergence of the results with a number M of slices as low as 10. In order to check for consistency of our results, we repeated the calculation with $M = 20$ and found no change in the thermal averages, within our statistical uncertainties.

In our PIMC calculation we neglected atomic exchanges, although they can be incorporated into the PIMC formalism [40, 42]. Their effect is negligible in neon.

It is important to note that PIMC allows us to calculate physical properties on a similar basis for *both* crystalline and liquid phases, at finite temperatures. We have studied the solid (FCC) phase of neon at the temperatures and densities corresponding to our experimental conditions (table 3); we computed the kinetic energy $\langle E_k(\rho, T) \rangle$ per particle and the pair distribution function $g(r)$.

In figure 5 and table 6 we compare our PIMC estimates for the kinetic energy with those obtained with both the Aziz HFD-C2 and the Lennard-Jones potential with theoretical results by Asger and Usmani [43], who used a Wigner–Kirkwood high-temperature expansion including terms up to \hbar^6 , and by Cuccoli *et al* [42], who performed a PIMC calculation.

The results of our calculation are in agreement with those reported by Cuccoli *et al* [42]; no significant difference arises from the use of a different potential, at least in the temperature and density regimes explored in this work. Such theoretical estimates are in agreement with the experimental data; this is an indication of the validity of a microscopic description based on a two-body potential. Many-body effects are known to affect significantly the equation

of state, particularly at high pressures; however, the kinetic energy is mostly affected by the repulsive hard core of the two-body part of the interaction potential, as a recent PIMC calculation for high-density helium has shown [44].

We also computed the pair distribution function $g(r)$; typical results are shown in figure 6, angle averaged for the FCC phase at $T = 20.2$ K. Well defined second- and third-nearest-neighbour peaks are present. We computed $g(r)$ with both the HFD-C2 and the Lennard-Jones potential; here too, no significant difference was found between the results obtained with the two potentials. The calculated pair distribution functions $g(r)$ were employed to determine $\langle \nabla^2 V \rangle$ from equation (17).

As the results reported in table 6 and figure 5 show, the kinetic energy estimates obtained by Asger and Usmani are significantly larger than those produced by the PIMC (as well as the experimental data), the difference being of the order of 4–5 K; moreover, their kinetic energies for the two potentials are significantly different with the HFD-C2 potential yielding a slightly larger kinetic energy value than the Lennard-Jones potential does. This raises some doubts about the convergence of the expansion, which is known to be rather slow when one is dealing with hard-core potential such as those of relevance here. On the other hand, PIMC estimates should be very accurate, given the size of the systems studied; on this point we note once again the agreement between our calculation and the independent calculation by Cuccoli *et al.*

The new PIMC FCC neon values were also included in figure 4. They are compared with the present values measured on eVS and the previous measurements on FCC neon made by Peek *et al.* [12]. Good agreement between the PIMC calculations and the eVS results is observed.

6. Conclusions

Measurements of $J(y)$ and hence $n(P)$ and $\langle E_k \rangle$ have been made for the simple system of solid neon at a number of temperatures between 4.25 and 20.2 K using two different spectrometer configurations. The agreement between data obtained at similar temperatures

Table 6. Calculated values of kinetic energy of FCC neon: WKE, Wigner–Kirkwood expansion.

Theoretical calculations					
Density (nm ⁻³)	Temperature (K)	$\langle E_k(\rho, T) \rangle$ (K) for the following potentials Aziz	Lennard-Jones	Method	Reference
44.97	4.125	41.6(1)	42.0(3)	PIMC	Present work
44.97	5.00	—	42.8(4)	PIMC	[42]
44.88	9.220	48.8(1)	—	WKE	[43]
44.87	9.370	—	49.8(2)	WKE	[43]
44.86	10.00	—	43.2(6)	PIMC	[42]
44.85	10.154	42.6(1)	43.2(1)	PIMC	Present work
44.74	12.02	—	49.8	WKE	[43]
44.73	12.10	52.8	—	WKE	[43]
44.48	15.00	—	44.7(7)	PIMC	[42]
44.48	15.687	46.5(1)	—	PIMC	Present work
44.26	17.97	54.5	—	WKE	[43]
44.26	18.09	—	51.3	WKE	[43]
43.78	20.00	—	47.7(9)	PIMC	[42]
43.50	20.308	47.8(1)	47.8(1)	PIMC	Present work

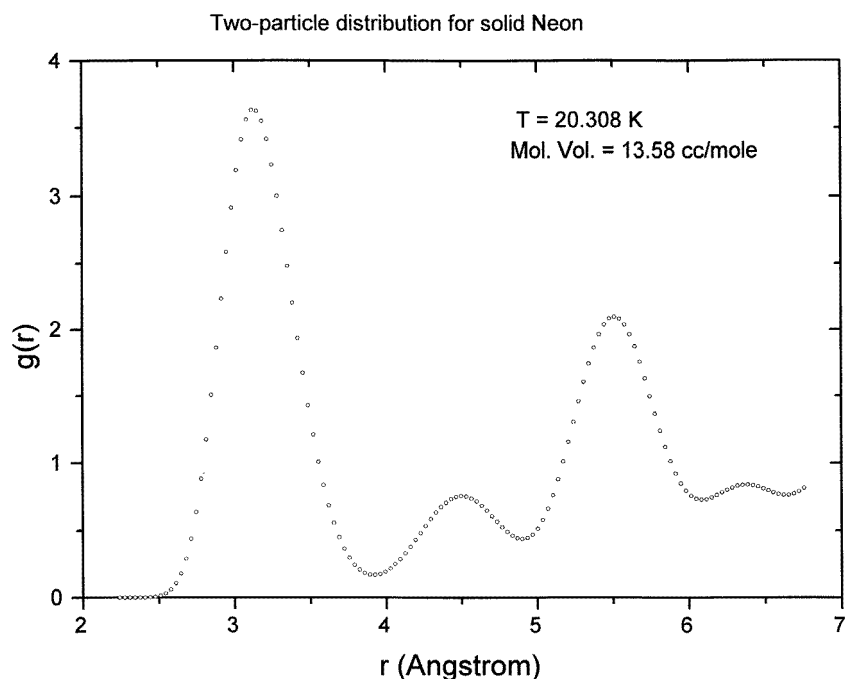


Figure 6. Angle-averaged pair distribution function $g(r)$ for FCC neon at $T = 20.2$ K, computed by PIMC (see section 5.1).

demonstrates that the data are free from systematic errors above the statistical accuracy of the measurements. We have considered the effects of multiple scattering on these data and have shown that they are below the statistical accuracy of these data and no correction was deemed necessary. Similarly, we have estimated FSEs to be small and no correction has been implemented.

The measured $\langle E_k \rangle$ are significantly lower than previous measurements by Peek *et al* and we list some possible contributions to systematic errors in their data analysis. From figure 4 we can estimate that the ground state in neon is reached at about 10–15 K, in agreement with the data of Peek *et al*.

PIMC calculations of solid neon kinetic energy were published by Cuccoli *et al* who used a Lennard-Jones pair potential. Good agreement is observed at all temperatures between their data and our PIMC calculations performed using both the Lennard-Jones and the Aziz potentials. This suggests that the mean kinetic energy is insensitive to the type of atomic potential used and we conclude that a two-body potential is sufficient to describe the atomic kinetic energy measured here. On the other hand, PIMC results for $\langle E_k \rangle$ are significantly lower than those obtained using a Wigner–Kirkwood expansion for the same two potentials. This demonstrates that the expansion, carried out to terms in \hbar^6 , is not convergent in the case of solid neon.

Acknowledgments

This research was supported in part by the UK Science and Engineering Research Council under contracts GR/H97161 and GR/H03919, in part by the US Department of Energy,

Basic Energy Sciences–Materials Sciences under contract DEFG02-91ER45439, and in part by the US National Science Foundation under grant no DMR 88-08126. We are pleased to acknowledge capable assistance by Ian Bailey, John Dreyer and the technical staff of ISIS.

References

- [1] Hohenberg P C and Platzmann P M 1966 *Phys. Rev.* **152** 198
- [2] Williams B (ed) 1977 *Compton Scattering* (New York: McGraw-Hill)
- [3] Sears V F 1971 *Phys. Rev. A* **5** 452; 1973 *Phys. Rev. A* **7** 340
Weinstein J J and Negele J W 1982 *Phys. Rev. Lett.* **49** 1016
- [4] Mayers J, Andreani C and Baciocco G 1989 *Phys. Rev. B* **39** 2022
- [5] Mayers J 1990 *Phys. Rev. B* **41** 41
- [6] Windsor C G 1981 *Pulsed Neutron Scattering* (London: Taylor and Francis)
- [7] Langel W E, Price D L, Simmons R O and Sokol P E 1988 *Phys. Rev. B* **38** 275
Herwig K W, Gavilano J C, Schmidt M C and Simmons R O 1990 *Phys. Rev. B* **41** 96
Mayers J 1993 *Phys. Rev. Lett.* **71** 1553
- [8] Postorino P, Fillaux F, Mayers J, Tomkinson J and Holt R S 1991 *J. Chem. Phys.* **94** 4411
- [9] Hilleke R O, Chaddah P, Simmons R O, Price D L and Sinha S K 1984 *Phys. Rev. Lett.* **52** 847
Bladsdell R C, Ceperley D M and Simmons R O 1993 *Z. Naturf. a* **48** 433
- [10] Mook H 1988 *Phys. Rev. B* **37** 5806
Snow W M, Yang Y and Sokol P E 1992 *Europhys. Lett.* **19** 403
Anderson K H, Stirling W G, Taylor A D, Bennington S M, Bowden Z A, Bailey I and Glyde H R 1992 *Physica B* **181** 865
- [11] Peek D A and Simmons R O 1991 *J. Chem. Phys.* **94** 3169
- [12] Peek D A, Fujita I, Schmidt M C and Simmons R O 1992 *Phys. Rev. B* **45** 9680
- [13] Peek D A, Schmidt M C, Fujita I and Simmons R O 1992 *Phys. Rev. B* **45** 9671
Fradkin M A, Zeng S X and Simmons R O 1994 *Phys. Rev. B* **49** 3197
- [14] Evans A C, Mayers J, Timms D N and Cooper M J 1993 *Z. Naturf. a* **48** 425
Fulton S, Cowley R A and Evans A C 1994 *J. Phys.: Condens. Matter* **6** 2977
Evans A C, Mayers J and Timms D N 1994 *J. Phys.: Condens. Matter* **6** 4197–212
- [15] Pauli M P and Holt R S 1988 *J. Phys. C: Solid State Phys.* **21** 3633
Rauh H and Watanabe N 1984 *Phys. Lett.* **100A** 244
- [16] Evans A C, Timms D N, Mayers J and Bennington S M 1996 *Phys. Rev. B* **53** 3023
- [17] Bernejo F J, Mompeán F J, Srinivasan A, Mayers J and Evans A C 1994 *Phys. Lett.* **189A** 333
- [18] Peek D A and Simmons R O 1991 *J. Chem. Phys.* **94** 3169
- [19] Lovesey S W 1984 *Theory of Neutron Scattering from Condensed Matter* (Oxford: Clarendon)
- [20] Sears V F 1984 *Phys. Rev. B* **30** 44
- [21] Evans A C, Mayers J, Timms D N and Cooper M J 1993 *Z. Naturf. a* **48** 415
Mayers J and Evans A C 1991 *Rutherford Appleton Laboratory Report RAL-91-048*
- [22] Mayers J and Evans A C 1991 *Rutherford Appleton Laboratory Report RAL-91-048*
- [23] Evans A C, Mayers J and Timms D N 1994 *J. Phys.: Condens. Matter* **6** 4197–212
- [24] Andreani C, Baciocco G, Holt R S and Mayers J 1989 *Nucl. Instrum. Methods A* **276** 297
- [25] Evans A C 1993 *PhD Thesis* University of Warwick
- [26] Mughabghab S F, Divadeenam M and Holden N E 1981 *Neutron Cross Sections* vol 1, part A (New York: Academic)
- [27] Mughabghab S F 1981 *Neutron Cross Sections* vol 1, part B (New York: Academic)
- [28] Chemically pure natural Ne from British Oxygen Company
- [29] AS Scientific Products Ltd, 2 Barton Lane, Abingdon OX14 3NB, UK
- [30] Batchelder D N, Losee D L and Simmons R O 1967 *Phys. Rev.* **162** 767
- [31] Holden N E 1992 *Handbook of Chemistry and Physics* ed D R Lide (Boca Raton, FL: CRC Press) pp 11–28
- [32] Sears V F 1986 *Methods of Experimental Physics. Neutron Scattering* vol 23, part A, ed K Sköld and D L Price (Orlando, FL: Academic) p 521
- [33] Sears V F 1988 *Phys. Rev. B* **30** 44
- [34] Buyers W L, Sears V F, Lonngi P A and Lonngi D A 1975 *Phys. Rev. A* **11** 697
- [35] Sears V F 1981 *Can. J. Phys.* **59** 555
- [36] Fradkin M A, Zeng S X and Simmons R O 1994 *Phys. Rev. B* **49** 3197

- [37] Ceperley D M and Pollock E L 1991 *Monte Carlo Methods in Theoretical Physics* ed S Caracciolo and A Fabrocini (Pisa: ETS Publishing)
- [38] Schmidt K E and Ceperley D M 1992 *The Monte Carlo Method in Condensed Matter Physics* ed K Binder (New York: Springer)
- [39] Ceperley D M and Pollock E L 1986 *Phys. Rev. Lett.* **56** 351
- [40] Aziz R A 1984 *Inert Gases: Potentials, Dynamics, and Energy Transfer in Doped Crystals* ed M L Klein (Berlin: Springer)
- [41] Brown J S 1966 *Proc. Phys. Soc.* **89** 987
- [42] Cuccoli A, Macchi A, Tognetti V and Vaia R 1993 *Phys. Rev. B* **47** 14923
- [43] Asger M and Usmani Q N 1994 *Phys. Rev. B* **49** 12262
- [44] Boninsegni M, Pierleoni C and Ceperley D M 1994 *Phys. Rev. Lett.* **72** 1854